Green

Production tracking information:

All boxes in the below coloured section need to be filled out and confirmed prior to export. Blue by EA, Green by Editor.

Manuscript Number	NCOMMS-16-20851B		
Received Date	1st Sept 2016	**OA License**	CC BY
MS# Double Publication	N	**Confirm License**	CC BY
Consortia (in Author List)	N	**Consortia Checked**	Y

Subject Ontology: Ontology paths as deep as possible, up to four terms	Physical sciences/Physics/Plasma physics/Astrophysical plasmas Physical sciences/Astronomy and planetary science/Space physics/Magnetospheric physics

Text to copy to the Export Field:

Author queries to add to Proof:

Items to pick up at Proof:

Notes to Sub/Typesetter:

The license type for this paper is CC BY.

Ref 1, page range is 405-406
Ref 3, page range is 1362-1365
Ref 14, page range is R1-R56

Editorial tracking information:

EA	
Editors	FL-DG
Corr. Author	Gershman
Date LTP Received	4th January 2017
Chinese Corr.	N
Japanese Corr.	N
US/UK/Canadian Gov. Corr.	N

ED	
Manuscript Title	Wave-particle energy exchange directly observed in a kinetic Alfvén-branch wave
Press Release	N
Hero Image	N
New Species	N
Novel Accession Codes	N

SI GUIDE

SI GUIDE

Type of file: pdf
Size of file: 437 KB
Title of file for HTML: Supplementary Information
Description: Supplementary Figures.

Type of file: pdf
Size of file: 0 KB
Title of file for HTML: Peer Review File
Description:

Wave-particle energy exchange directly observed in a kinetic Alfvén-branch wave

Daniel J. Gershman*[1,2], Adolfo F-Viñas[2], John C. Dorelli[2], Scott A. Boardsen[2,3], Levon A. Avanov[1,2], Paul M. Bellan[4], Steven J. Schwartz[5], Benoit Lavraud[6,7], Victoria N. Coffey[8], Michael O. Chandler[8], Yoshifumi Saito[9], William R. Paterson[2], Stephen A. Fuselier[10], Robert E. Ergun[11], Robert J. Strangeway[12], Christopher T. Russell[12], Barbara L. Giles[2], Craig J. Pollock[2], Roy B. Torbert[13,14], and James L. Burch[10]

(1) Department of Astronomy, University of Maryland, College Park, MD, 20742
(2) NASA Goddard Space Flight Center, Greenbelt, MD, 20771
(3) Goddard Planetary Heliophysics Institute, University of Maryland, Baltimore County, MD, 21250
(4) Division of Engineering and Applied Science, California Institute of Technology, Pasadena CA, 91125
(5) Blackett Laboratory, Imperial College London, London SW7 2AZ, UK
(6) Institut de Recherche en Astrophysique et Planétologie, Université de Toulouse, France
(7) Centre National de la Recherche Scientifique, UMR 5277, Toulouse, France
(8) NASA Marshall Space Flight Center, Huntsville, AL, 35808
(9) JAXA Institute of Space and Astronautical Science, Sagamihara, Kanagawa 252-5210, Japan
(10) Southwest Research Institute, San Antonio, TX, 78238
(11) Astrophysical and Planetary Sciences, University of Colorado, Boulder, CO, 80305
(12) Department of Earth, Planetary, and Space Sciences, University of California, Los Angeles, CA, 90095
(13) Physics Department, University of New Hampshire, Durham, NH, 03824
(14) Southwest Research Institute Durham, Durham, NH, 03824

* Corresponding author (daniel.j.gershman@nasa.gov)

Abstract. Alfvén waves are fundamental plasma wave modes that permeate the universe. At small kinetic scales they provide a critical mechanism for the transfer of energy between electromagnetic fields and charged particles. These waves are important not only in planetary magnetospheres, heliospheres, and astrophysical systems, but also in laboratory plasma experiments and fusion reactors. Through measurement of charged particles and electromagnetic fields with NASA's Magnetospheric Multiscale (MMS) mission, we utilize Earth's magnetosphere as a plasma physics laboratory. Here we confirm the conservative energy exchange between the electromagnetic field fluctuations and the charged particles that comprise an undamped kinetic Alfvén wave. Electrons confined between adjacent wave peaks may have contributed to saturation of damping effects via non-linear particle trapping. The investigation of these detailed wave dynamics has been unexplored territory in experimental plasma physics and is only recently enabled by high-resolution MMS observations.

Introduction

The Alfvén wave is a ubiquitous plasma wave mode wherein ions collectively respond to perturbations in the ambient magnetic field direction[1]. No net energy is transferred between the field and the plasma particles in ideal Alfvén waves. However, ion motion decouples from electron motion when wave dynamics are faster than ion orbital motion around the local magnetic field or are on scales smaller than the ion orbit size, defined by the gyrofrequency (ω_{ci}) and gyroradius (ρ_i), respectively. When the perpendicular spatial scale of an Alfvén wave approaches ρ_i, the wave can support significant parallel electric and magnetic field fluctuations that enable net transfer of energy between the wave field and plasma particles via Landau or transit-time interactions[2-4].

The transition of an ideal fluid-scale Alfvén wave to a kinetic-scale Alfvén wave (KAW) occurs at $k_\perp \rho_i \sim 1$ and $k_\perp > k_\|$, where **k** is the wave vector and '$\perp$' and '$\|$' are defined with respect to the local magnetic field direction. These KAWs are essential for energy transfer processes in plasmas. Broadband KAWs have long been associated in space physics with turbulent heating in the solar wind and magnetosheath[5-7], and are also thought to account for a substantial amount of the energy input into Earth's auroral regions that can drive charged particle outflow and atmospheric loss[8-13]. In the laboratory, KAWs can transport energy away from the core regions of fusion plasmas, resulting in the unwanted deposition of energy at the reactor edges[14,15]. Understanding kinetic-scale wave generation, propagation, and interaction with charged particles is critical to unraveling and predicting the relevant physics of these fundamental processes.

Alfvén wave theory predicts that transverse fluctuations in the current density (**J**) and electron-pressure-gradient-driven electric field ($\mathbf{E}_p = -\nabla \bullet \underline{\mathbf{P}}_e/(n_e e)$) are 90° out of phase with one another, such that the plasma heating term, $\Delta(J_\perp E_{p\perp})$, can be instantaneously non-zero but averages to zero over a wave period[1]. In such an undamped wave, power sloshes back and forth between the wave-field and particles with no net energy transfer. There are no corresponding fluctuations in $\Delta E_{p||}$ and $\Delta J_{||}$ in an ideal Alfvén wave. For kinetic-scale Alfvén waves, however, non-zero $\Delta E_{p||}$ fluctuations enable the Landau resonance, where particles with $V_{||} \sim \omega/k_{||}$ can gain or lose energy through interaction with the wave field. These interactions, combined with an imbalance in the number of particles that are moving faster than or slower than the wave, result in net plasma heating or cooling[4]. Here, fluctuations in $\Delta J_{||}$ and $\Delta E_{p||}$ become in-phase such that the wave-averaged $\Delta(J_{||}E_{p||})$ is non-zero[3,16]. Likewise, fluctuations in $\Delta B_{||}$ result in transit-time damping effects, the magnetic analog of Landau damping, where the magnetic mirror force takes the place of $\mathbf{E}_p$[2,4]. For non-linear KAWs, parallel fluctuations can be sufficiently large in amplitude to trap electrons between adjacent wave peaks. The oscillatory bounce motion of these electrons produces equal numbers of particles moving faster than or slower than the wave, limiting the effects of Landau and transit-time damping, and enabling stable wave mode propagation[4,17].

The detailed properties of KAWs (e.g., $\Delta\mathbf{J}$, $\Delta\mathbf{E}_p$, $\mathbf{k}$) have been difficult to characterize due to their small spatial and temporal scales with respect to the capabilities of laboratory or on-orbit plasma instrumentation. Accurate estimates of current density and the characterization of particle populations require full three-dimensional distribution functions of both electron and ions on time-scales faster than the wave frequency in the observation frame of reference. In addition, estimates of pressure gradients and wavevectors rely on multiple observation points being available within a single wave peak. However, NASA's recently launched Magnetospheric Multiscale (MMS) mission[18] consists of four identical observatories deployed in a tetrahedron configuration that measure charged particle and electromagnetic fields orders of magnitude more quickly than previous space missions. This increased temporal sampling combined with a small MMS inter-spacecraft separation enables plasma parameters and their spatial gradients to be determined at kinetic scales.

Here we use observations from MMS to characterize the microphysics of a monochromatic Alfvén wave. Through the calculation of $\Delta\mathbf{J}\bullet\Delta\mathbf{E}$, we provide a direct measurement of the conservative energy exchange between the wave's electromagnetic fields and particles. A perpendicular spatial scale of $k_\perp\rho_i \sim 1$, non-zero $\Delta E_{p||}$ and $\Delta J_{||}$ fluctuations, and a parallel wave speed close to the local Alfvén speed confirm that the wave packet is an ion-scale KAW. Finally, analysis of the velocity distribution function of electrons reveals a population that is non-linearly trapped within the wave's magnetic minima. These trapped electrons may have enabled non-linear saturation of damping processes, resulting in marginally stable wave propagation and providing evidence in support of early analytical theories of wave-particle interactions in collisionless plasmas.

Results

Event Overview. On 30 December 2015 the four MMS observatories were near the dayside magnetopause i.e., the interface between the interplanetary magnetic field and the Earth's internal magnetic field, at [7.8, -6.9, 0.9] R_e (1 R_e = 1 Earth radius = 6730 km). Magnetic reconnection at the magnetopause boundary[19,20] generated a southward flowing exhaust at ~22:25 UT denoted by a $-V_z$ jet, an increase in plasma density, and a decrease in plasma temperature [see Fig. 1]. There was no discernable rotation in the magnetic field suggesting that the spacecraft constellation remained inside the Earth's magnetosphere throughout this interval. Low frequency (~1 Hz) waves were observed in the exhaust in a ~4 min interval localized to a region of strong proton temperature anisotropy ($T_{H+\perp}/T_{H+\|} \sim 2$). MMS partially crossed the magnetopause into the magnetosheath for the first time at ~ 22:35 UT (not shown) at [8.0,-6.9,0.9] R_e. For the subsequent ~2 hours, multiple magnetopause crossings resulted in the MMS spacecraft sampling both $+V_z$ and $-V_z$ jets, i.e., above and below the reconnection site. However, ~1 Hz waves were only observed in the short interval shown in Figure 1. The MMS observatories were in a tetrahedron configuration (quality factor[21] ~0.9) separated by ~40 km, a distance which corresponded to a local thermal ion gyroradius (ρ_i = 35 km).

The reconnection exhaust plasma consisted of mostly H^+ and some He^{2+} with number density ratio n_{He2+}/n_{H+} less than 0.02 throughout the interval. The local ratios of ion thermal parallel and perpendicular pressure to magnetic pressure were $\beta_\| \approx 0.2$ and $\beta_\perp \approx 0.5$, respectively. In addition, the average plasma flow velocity during this interval was $\mathbf{V_o}$ = [-17,73,-183] km s^{-1}. This velocity corresponded to a jet flowing nearly anti-parallel to the background magnetic field ([0.10, -0.52, 0.85] direction) with speed ~0.5 V_A, where V_A is the Alfvén speed i.e., the characteristic speed in which information can be transferred along a magnetic field. For this interval, with n_{H+} = 10 cm^{-3} and B = 55 nT, the local Alfvén speed was estimated to be 380 km s^{-1}. Variations were observed in the number density (Δn), bulk velocity ($\Delta \mathbf{v_e}$), temperature ($\Delta T_\|$, $\Delta T_\perp$) of both ions and electrons, and in the electric ($\Delta\mathbf{E}$) and magnetic fields ($\Delta\mathbf{B}$) [see Fig. 2]. The amplitude of these ~1 Hz fluctuations were non-linear with $\Delta n_{H+}/n_{H+} \sim 0.2$. The magnetic field fluctuations exhibited both left-handed and right-handed polarization [see Supplementary Figure 1]. Finally, bursts of electron phase space holes measured in the total parallel electric field ($\Delta E_\|$) were bunched with the wave in locations of strong electron pressure gradients.

Wave Properties. Accurate determination of the wavevector (**k**) was critical to identify the observed wave mode. *In situ* estimation of **k**, especially for broadband wave spectra, is non-trivial, and often relies on multi-spacecraft[22.] Fortunately, the monochromatic nature of the observed wave enabled the application of several independent methods of wavevector determination. Here we utilized four methods to provide a robust estimate of **k**: (1) parallel component of the wavevector derived from the correlation between velocity and magnetic field fluctuations[16], (2) **k**-vector estimation from current and magnetic field fluctuations measured in the spacecraft frame[23,24], (3) comparison of spacecraft-measured gradients with their corresponding spacecraft-averaged quantities, i.e., the plane-wave approximation[4], and (4) phase differencing of the magnetic field fluctuations between each spacecraft[25].

In the first method we estimated the parallel component of the wavevector through comparison of four-spacecraft-averaged electron velocity and magnetic field fluctuations. Alfvén-branch waves have parallel wave speeds close to the local Alfvén speed, i.e., $|\omega/k_{\parallel}| \approx V_A$ and correlated transverse fluctuations[16], $\Delta\mathbf{V}_{\mathbf{e}\perp} = -(\omega/k_{\parallel})\Delta\mathbf{B}_{\perp}/B$. Positively-correlated ($R^2 = 0.92$) $\Delta\mathbf{V}_{\mathbf{e}\perp}$ and $\Delta\mathbf{B}_{\perp}$ indicated that $\omega/k_{\parallel} = -1.15\pm0.03\ V_A$, i.e., the wave propagated anti-parallel to the background magnetic field near the Alfvén speed [see Supplementary Fig. 2]. Although qualitatively similar ~1 Hz fluctuations have been observed near Earth's bow shock that are more consistent with magnetosonic wave modes[26], a parallel phase speed well above the local sound speed of $\sim0.5\ V_A$ and the anti-correlation between density and magnetic field fluctuations were inconsistent with slow and fast magnetosonic wave modes, respectively.

In the second method we combined fluctuations of current and magnetic field in the spacecraft frame to estimate **k** as a function of frequency using spectral techniques recently developed by *Bellan*[23,24]. Here, the **k**-vector was derived directly from fluctuations in $\Delta\mathbf{J}$ and $\Delta\mathbf{B}$ measured in the spacecraft frame [see Fig. 3]. Although this technique could have been applied to data from a single spacecraft, in order to maximize spectral resolution we used the four-spacecraft average of $\Delta\mathbf{B}$ and the average $\Delta\mathbf{J}$ determined from magnetometer data using the four-spacecraft 'curlometer' technique[27]. The value of **k** at the frequency of maximum spectral power, 0.9 Hz, was $\mathbf{k} = [7.1\text{x}10^{-3}, -2.0\text{x}10^{-2}, -2.2\text{x}10^{-2}]\ \text{km}^{-1}$, which corresponded to a wavevector angle (θ) of $\sim100^{\circ}$ with respect to the background magnetic field and $k_{\perp}\rho_i \sim 1.0$.

In the third method we used the phase difference[25] measured between each pair of MMS spacecraft for each component of the magnetic field to derive additional estimates of **k**. At the spectral peak of 0.9 Hz, the **k**-vector determined from the phase-differencing of the B_X, B_Y, and B_Z fluctuations (using MMS3 as a reference) were: $[-7.4\text{x}10^{-5}, -8.5\text{x}10^{-3}, -1.5\text{x}10^{-2}]\ \text{km}^{-1}$, $[2.9\text{x}10^{-2}, 4.7\text{x}10^{-3}, -1.1\text{x}10^{-2}]\ \text{km}^{-1}$, and $[2.3\text{x}10^{-2}, -3.5\text{x}10^{-3}, -1.0\text{x}10^{-2}]\ \text{km}^{-1}$ respectively. Although similar phase shifts were observed in all components of $\Delta\mathbf{B}$ between MMS2, MMS3, and MMS4, there were significantly different shifts of MMS1 with respect to the other observatories for each component [see Supplementary Fig. 3]. These differences demonstrated that this wave packet was not truly planar and exhibited spatial structure on the order of an ion gyroradius. Because MMS1 was farthest from the magnetopause (i.e., the X direction), the k_X component was most strongly affected by this structure. Despite this discrepancy, all determinations of **k** result in $k_{\perp}\rho_i \sim 1$ and the phase differencing of B_X and B_Y components, those with the largest fluctuation power, both produced $\omega/k_{\parallel} = -1.1\ V_A$.

Finally, in the fourth method, the small MMS spacecraft separations and high quality tetrahedron formation enabled gradients of particle and field quantities to be estimated directly from MMS data. These gradients were compared with those predicted by the plane-wave approximation (i.e., '$\nabla\bullet$'$\approx i\mathbf{k}$ and '$\nabla\times$'$\approx i\mathbf{k}\times$ at a single frequency[4]) to both evaluate the validity of this approximation to the observed wave packet and to provide further validation of **k** [see Fig. 4]. The current was calculated from three methods: (1) direct particle observations, i.e., $en_e(\mathbf{V}_i-\mathbf{V}_e)$, (2) magnetic field 'curlometer'[27], i.e., $\nabla\times\mathbf{B}/\mu_o$, and (3) the plane-wave approximation, i.e., $i\mathbf{k}\times\mathbf{B}/\mu_o$. All three estimates of $\Delta\mathbf{J}$ are shown in Figure 4. k_y and k_z most strongly influenced the plane-wave derived currents such that this intercomparison was relatively insensitive to errors in the determination of k_x. The electron-pressure-gradient-driven electric field determined from four spacecraft measurements (i.e., $-\nabla\bullet\underline{\underline{\mathbf{P}}}_e/(n_e e)$), when compared with its plane-wave approximated value (i.e., $-\,i\mathbf{k}\bullet\underline{\underline{\mathbf{P}}}_e/(n_e e)$), provides further confidence in the determination of **k** [see Fig. 4]. Here, all three components of **k** contributed to this result. The *X*-component comparison demonstrates that k_x is of the correct sign but may underestimate the four-spacecraft gradient.

We adopted the **k-**vector derived using the *Bellan*[23,24] method $\mathbf{k} = [7.1\mathrm{x}10^{-3}, -2.0\mathrm{x}10^{-2}, -2.2\mathrm{x}10^{-2}]$ km^{-1} because it simultaneously leveraged data from all four spacecraft and all components of the magnetic field. Allowing for ~30% (3-σ level) uncertainty in each individual component, we found $k_\perp\rho_i = 1.02\pm0.07$ with wavevector angle 104 ± 4^o from the magnetic field. The 0.9 Hz peak observed in the spacecraft frame (ω_{sc}) was then Doppler-shifted by $\omega = \omega_{sc} - \mathbf{k}\bullet\mathbf{V_o}$ to obtain a frequency of $\omega/\omega_{ci,H+} = 0.61\pm0.08$ in the plasma frame. We conclude that multiple independent methods indicated that MMS resolved a kinetic-scale Alfvén branch wave.

Modeled Wave Growth Rates. Growth rates ($\gamma = \mathrm{Im}\{\omega/\omega_{ci}\}$) and polarization ($\mathrm{Re}\{iE_y/E_x\}$) solutions along the Alfvén-branch dispersive surface were estimated using a linear dispersion solver and are shown as a function of θ in Figure 5. The dispersion solver predicted that the large ion temperature anisotropy of $T_{i\perp}/T_{i||} \sim 2$ produced a nearly monochromatic ion cyclotron wave mode that propagated parallel/anti-parallel to the background magnetic field ($\theta = 0^o, 180^o$) with $\omega/\omega_{ci} \sim 0.5$, $k\rho_i \sim 0.4$ and left-handed polarization. At increasingly oblique wavevector angles, the predicted wave growth was substantially reduced. There was no slow or fast magnetosonic wave growth predicted for the measured plasma parameters. Several Alfvén-branch dispersion curves are shown in Figure 5 as a function of $k\rho_i$ and θ. The observed KAW mode ($\omega/\omega_{ci} = 0.6$, $k\rho_i = 1$, $\theta = 100^o$) was close to, but not precisely on the solution surface. Nearby Alfvénic solutions to the measured data (matching two of the three wave parameters) were $\{\omega/\omega_{ci} = 0.3, k\rho_i = 1, \theta = 100^o\}$, $\{\omega/\omega_{ci} = 0.6, k\rho_i = 1.6, \theta = 100^o\}$, and $\{\omega/\omega_{ci} = 0.6, k\rho_i = 1, \theta = 110^o\}$. All of these nearby solutions were weakly damped ($|\gamma| \sim 10^{-2}$) such that local generation of the observed KAW was not predicted by linear wave theory. However, local spatial gradients of plasma density may have increased the θ of the ion cyclotron mode during its propagation, converting it into an oblique Alfvén wave[4]. Furthermore, non-linear effects and parametric forcing (e.g., magnetopause motion), were not taken into account by the homogenous dispersion solver, yet may have played a role in the evolution of the observed KAW.

Wave-Particle Interactions. Given the demonstrated validity of the plane-wave approximation for $\Delta\mathbf{E}_p$, the electron-pressure-gradient-driven electric field was estimated at a single spacecraft, e.g., MMS4, using $-i\mathbf{k}\bullet\underline{\underline{\mathbf{P}}}_e/(n_e e)$. Fluctuations of $\Delta\mathbf{E}_p$ and $\Delta\mathbf{J}$ in magnetic coordinates on MMS4 are shown in Figure 6. In addition to the transverse electric-field fluctuations expected for all Alfvén waves, fluctuations in $\Delta E_{p||}$ further confirmed the presence of kinetic-scale effects. These parallel fluctuations were an order of magnitude smaller than those in $\Delta E_{p\perp}$ as expected from KAW theory[16]. Furthermore, fluctuations in all components of $\Delta\mathbf{J}$ and $\Delta\mathbf{E_p}$ (both perpendicular and parallel) were each ~90° out-of-phase with one another. These phase differences resulted in a non-zero instantaneous value of $\Delta(\mathbf{J}\bullet\mathbf{E_p})$with $\Delta\,|\mathbf{J}\bullet\mathbf{E}_p|_{max} \approx 50$ pW m^{-3} and near-zero wave-averaged $\Delta(J_\perp E_{p\perp})$and $\Delta(J_{||}E_{p||})$quantities. These data demonstrated the conservative energy exchange between the particles and fields that comprise an undamped KAW.

Because $k_\perp\rho_e << 1$, electrons should have remained magnetized throughout the wave packet. Close examination of the electron velocity distribution function in the parallel wave frame revealed three distinct populations of electrons in the wave packet: (1) an isotropic thermal core, (2) suprathermal beams counterstreaming along the magnetic field, and (3) trapped particles with near ~90° magnetic pitch angles (Fig. 7). Thermal and counterstreaming electrons are commonly observed in the magnetopause boundary layer in the absence of analogous wave activity[28]. However, trapped electron distributions are atypical of ambient boundary layer plasmas. Furthermore, these trapped electrons were dynamically significant: they accounted for ~50% of the density fluctuations within the KAW. Although these electrons also resulted in a ~20% increase in $T_{e\perp}$, they were not indicative of heating but rather of a non-linear capture process.

The depth of the parallel potential well was estimated from $\Delta E_{p||}$ and $k_{||}$ to be ~10V [Fig. 7]. In addition, the parallel magnetic field of the wave generated a mirror force that resulted in a kinetic-scale magnetic bottle between successive wave peaks. This mirror force supplemented the force from the wave's parallel electric field, enabling trapping of electrons with magnetic pitch-angles between ~75° and ~105° (B_{min}/B_{max}=0.96). To understand the combined effects of these forces, electrons measured in the magnetic minima were Liouville-mapped to other locations along the wave using various parallel potential well depths [Figure 8]. The full-width at half maximum distance along the wave at a pitch-angle of 90° was calculated for each potential and compared with the measured data. The best match between measured and Liouville-mapped distributions was found for a potential well depth of $|\Phi_{max}|$=10V. Such agreement provided additional validation of $\Delta \underline{E}_{\mathrm{p}\|}$ and $k_{\|}$. In addition, these distributions demonstrated that the effect of the parallel electric field was to confine magnetically trapped electrons closer to magnetic minima.

Discussion

KAWs in turbulent space plasmas are thought to account for heating of plasmas at kinetic scales[5-7]. In previous studies[29,30], such waves were found to have $k_{\perp} \gg k_{\|}$, i.e., $\theta \sim 90^{\circ}$. This plasma heating was accompanied by significant reductions in field fluctuation power. The wave presented here had a somewhat higher frequency ($\omega_{\mathrm{ci,He2+}} < \omega < \omega_{\mathrm{ci,H+}}$) than those considered in these previous KAW studies ($\omega \ll \omega_{\mathrm{ci,H+}}, \omega_{\mathrm{ci,He2+}}$). Furthermore, its comparatively non-perpendicular wavevector ($\theta \approx 100^{\circ}$) and large scale ($k_{\perp}\rho_{\mathrm{i}} \approx 1$) indicated that the observed wave was close to the transition point between ideal and kinetic regimes. Nonetheless, the wave had non-zero $\Delta J_{\|}$ and $\Delta E_{\mathrm{p}\|}$ fluctuations, confirming that it contained kinetic-scale structure not present in an ideal Alfvén wave. These observations demonstrated that the mere presence of a KAW or parallel electric field fluctuations do not necessarily imply heating via Landau damping. Only in-phase fluctuations in $\Delta \mathbf{J}$ and $\Delta \mathbf{E}_{\mathbf{p}}$ result in such net transfer of energy from the wave-field to the plasma particles.

In linear KAW theory, the electrostatic field formed by parallel gradients in electron pressure enables the energization of particles via the Landau resonance[4,13,16]. Similarly, the transit-time resonance becomes relevant for systems where there are parallel gradients in magnetic field magnitude. Despite the presence of these field gradients in the observed KAW, out-of-phase $\Delta E_{\mathrm{p}\|}$ and $\Delta J_{\|}$ fluctuations and a finite wave amplitude for several wave periods (i.e., $|\gamma| \ll 1$) indicated the absence of strong wave growth or damping. Although a hot core population ($V_{\mathrm{th,e}} \gg |\omega/k_{\|}|$) does not lead to strong damping [Fig 5.], the velocity distribution function of electrons was not directly sampled at energies corresponding to $V_{\|} \sim \omega/k_{\|}$, (i.e., ~0.5 eV). Electrons at these low energies are often present as they serve to neutralize a ubiquitous population of ‘hidden' cold ions that flow out from the ionosphere[31]. Such ionospheric electrons may have added structure to the velocity distribution function near $V_{\|} \sim \omega/k_{\|}$, amplifying damping rates. However, non-linear KAW theories have predicted that trapped electrons with $V_{\|} \sim \omega/k_{\|}$ lead to wave stabilization if their bounce frequency (ω_{B}) is significantly faster than the damping or growth rate, i.e., $\omega_{\mathrm{B}}/\omega_{\mathrm{ci}} \gg |\gamma|$[4,17,32]. We estimated $\omega_{\mathrm{B}}/\omega_{\mathrm{ci}} \sim 1$ for this wave, consistent with such a criterion. Therefore, the presence of trapped electrons here could have contributed to non-linear instability saturation in a single-mode wave even if there were low energy structure in the electron distribution function that was not resolved by MMS.

Finally, at higher frequencies (~1 kHz), fluctuations in the total parallel electric field $\Delta E_{\|}$ associated with electron phase space holes[33] were bunched in phase with the low frequency wave packet (Fig 1). Because these structures persisted outside of the KAW interval (not shown), it is unlikely that they were related to its initial generation. However, the location of these electron-scale structures within the wave was coincident with the location of electron pressure gradients, suggesting that they could have contributed, in an average sense, to some of the observed ion-scale $\Delta E_{p||}$ fluctuations. Furthermore, electron holes may have been responsible for higher frequency contributions to $\Delta(J_{||}E_{||})$ in the form of non-linear and turbulent terms in the electron momentum equation[34].

Using MMS data we have experimentally confirmed the conservative energy exchange between an undamped kinetic Alfvén wave field and plasma particles: fluctuations of all three components of $\Delta\mathbf{J}$ and $\Delta\mathbf{E_p}$ were 90° out-of-phase with one another, leading to instantaneous non-zero $\Delta(\mathbf{J}\bullet\mathbf{E}_\mathrm{p})$**.** Furthermore, we have discovered a significant population of electrons trapped within adjacent wave peaks by the combined effects of the parallel electron-pressure-gradient-driven electric field and the magnetic mirror force. In addition to contributing ~50% of the density fluctuations in the wave, these trapped electrons may have provided non-linear saturation of Landau and transit-time damping. The monochromatic nature of the wave enabled a direct comparison of observations with linear and non-linear KAW theories. It is crucial to understand these dynamics to predict the evolution of kinetic-scale waves in laboratory fusion reactors, planetary magnetospheres, and astrophysical plasmas.

Methods

Coordinate Systems. The coordinate system used in this study (unless otherwise noted) was the Geocentric Solar Ecliptic (GSE) coordinate system, where the *X*-direction pointed towards the Sun along the Earth-Sun line, the *Z*-direction was oriented along the ecliptic north pole, and the *Y*-direction completed the right-handed coordinate system[35]. Local 'magnetic coordinates' were derived from GSE vectors where $\mathbf{B_3}$ was parallel to the local magnetic field direction, $\mathbf{B_1}$ was in the $\mathbf{X}_{\mathrm{GSE}} \times \mathbf{B}_3$ direction, and $\mathbf{B_2}$ completed the right-handed coordinate system, i.e., $\mathbf{B}_1 \times \mathbf{B}_2 = \mathbf{B}_3$.

Calculation of Plasma Parameters. The thermal gyroradius was calculated using

$$\rho_{\mathrm{i}} = \frac{m_{\mathrm{H+}}\sqrt{\frac{k_{\mathrm{B}}T_{\mathrm{H+}\perp}}{m_{\mathrm{H+}}}}}{eB} \qquad (1)$$

where k_{B} is Boltzmann's constant, e is the elementary charge, and $m_{\mathrm{H+}}$ is the mass of H^{+}. The ion gyrofrequency was calculated using,

$$\omega_{\mathrm{ci}} = \frac{eB}{m_{\mathrm{H+}}} \qquad (2)$$

The plasma thermal pressure was calculated using $n_{\mathrm{H+}}k_{\mathrm{B}}T_{\mathrm{H+}}$. The magnetic pressure was calculated using $B^2/2\mu_{\mathrm{o}}$ where μ_{o} is the magnetic permeability of free space. Finally, the Alfvén speed was calculated using

$$V_{\mathrm{A}} = \frac{B}{\sqrt{\mu_o n_{\mathrm{H+}} m_{\mathrm{H+}}}} \qquad (3)$$

All calculations were done in SI units.

$\Delta\mathbf{V}_{\mathrm{e}}$-$\Delta\mathbf{B}$ correlations. The comparison of $\Delta\mathbf{V}_{\mathrm{e}}$ and $\Delta\mathbf{B}$ was done in the direction of minimum current density fluctuations ([0.93,0.32,0.18]) such that ion and electron velocities were approximately equal. This minimum variance direction was nearly perpendicular to the background magnetic field direction $\mathbf{b}$ = [0.10, -0.52, 0.85].

Electric Field Measurements. The electric field in the electron frame was defined as $\mathbf{E}+\mathbf{V}_{\mathrm{e}}\times\mathbf{B}$, where $\mathbf{E}$ was the measured electric field in the ion frame[23]. Since $\mathbf{J}$ is frame-independent, this electron-frame electric field is conveniently used for estimates of energy transfer, i.e., plasma heating occurs when $\mathbf{J}\bullet(\mathbf{E}+\mathbf{V}_{\mathrm{e}}\times\mathbf{B}) > 0$. At the scales relevant for this KAW packet, electrons remained magnetized such that electron inertia and anomalous resistivity contributions to the electric field were neglected and the pressure gradient term should have been the dominant contributor to $\mathbf{E}+\mathbf{V}_{\mathrm{e}}\times\mathbf{B}$ at low frequencies. The individual amplitudes of $\mathbf{E}$ and $\mathbf{V}_{\mathrm{e}}\times\mathbf{B}$ were measured to be on the order of several mV m^{-1}. Systematic uncertainty in both particle and fields measurements would have led to a challenging recovery of $\mathbf{E}+\mathbf{V}_{\mathrm{e}}\times\mathbf{B}$ because $|\mathbf{E}+\mathbf{V}_{\mathrm{e}}\times\mathbf{B}| \ll |\mathbf{E}|,|\mathbf{V}_{\mathrm{e}}\times\mathbf{B}|$. Therefore, accurate direct estimates of $\mathbf{J}\bullet(\mathbf{E}+\mathbf{V}_e\times\mathbf{B})$ were not recovered for this event. Instead, here we focused on effects of the electric field generated by the divergence of the electron pressure tensor, i.e., $\mathbf{E}_p = -\nabla\bullet\underline{\underline{\mathbf{P}}}_e/(n_e e)$ and validated the measurement using multiple methods. In the electron frame, the electrons are not moving so there is no magnetic term in the electron equation of motion giving $\mathbf{E} \approx \mathbf{E}_p$.

Linear Instability Analysis. To determine the properties of kinetic modes that interact with ions and electrons at their respective scales we used the linear dispersion solver PLADAWAN[36] (PLAsma Dispersion And Wave ANalyzer) to solve the linearized Vlasov-Maxwell system for arbitrary wavevector directions. Using measured plasma parameters of ions and electrons, the dispersion solver produced growth rates and wave properties as functions of ω and $\mathbf{k}$. The plasma parameters used as input to the dispersion solver (assuming stationary plasma) were $n_{e-} = 10$ cm^{-3}, $B = 55$ nT, $T_{e\perp} = T_{e||} = 35$ eV, $T_{H+||} = 175$ eV, and $T_{H+\perp} = 350$ eV. Wave polarization was calculated using the simulated electric field fluctuations as $\mathrm{Re}\{iE_x/E_y\}$. Left-hand and right-hand polarization corresponded to $\mathrm{Re}\{iE_x/E_y\} < 0$ and $\mathrm{Re}\{iE_x/E_y\} > 0$, respectively[4]. No growth was observed for the slow-mode or fast-mode magnetosonic branches of the dispersion relation. Additional simulations were run to evaluate the influence of He^{2+} on the observed instability. Increased n_{He2+}/n_{H+} ratios up to 0.02 with $T_{He2+} = 550$eV reduced the maximum wave growth but did not alter the sharpness of the peak in k-space. No new wave modes appeared to be introduced into the system from the presence of the local He^{2+} population.

Liouville Mapping and Electron Bounce Motion. Under the assumption that electron phase space density $f(\mathbf{v})$ was conserved along particle trajectories throughout the wave interval (i.e., Liouville's theorem), we used $f(\mathbf{v})$ measured in the magnetic minimum, defined as $f_o(\mathbf{v})$, a sinusoidal profile of the magnetic field strength B with $M = B_{min}/B_{max} = 0.96$, and a sinusoidal profile of electric potential Φ to infer the velocity distribution along the wave[37,38]. Velocity space was transformed using equations,

$$v_{||o} = \pm\sqrt{v_\perp^2(D)\left(1-\frac{B_o}{B(D)}\right) + v_{||}^2(D) - \frac{2e}{m_e}\Phi(D)}, \tag{4}$$

and

$$v_{\perp o} = \sqrt{v_\perp^2(D)\left(\frac{B_o}{B(D)}\right)}, \tag{5}$$

where the 'o' subscripts denote values at the magnetic minimum of the wave. The '+' and '-' branches of equation (4) correspond to the sign of $v_{||}$. For each $(v_{||}, v_\perp)$ point in the reconstructed skymap, equations (4) and (5) provided a point $(v_{||o}, v_{\perp o})$ that was used to map a phase space density in the reference distribution, i.e., $f(v_{||}, v_\perp) = f_o(v_{||o}, v_{\perp o})$.

In the magnetic minimum ($D = \lambda_{||}/2$), $\frac{B_0}{B(D)} = 1$ and $\Phi = \Phi_o = 0$. At the magnetic maximum ($D = 0, \lambda_{||}$), $\frac{B_0}{B(D)} = M$ and $\Phi = -|\Phi_{\max}|$, i.e.,

$$\frac{B_0}{B(D)} = M + (1 - M)\sin(\frac{\pi}{\lambda_{||}} D) \qquad (6)$$

$$\Phi(D) = -\frac{|\Phi_{\max}|}{2}\left(1 + \cos\left(\frac{2\pi}{\lambda_{||}} D\right)\right). \qquad (7)$$

Finally, bounce frequencies ($\omega_B = 1/\tau_B$) for trapped electrons were estimated using,

$$\tau_B = 4\int_{\lambda_{||}/2}^{R} \frac{dD}{v_{||}\,(D)}, \qquad (8)$$

where R was defined as the reflection point along the wave ($i.e., v_{||}\ (R) = 0$). Electrons with pitch angles 75-90^o and energies 100-400eV produced bounce frequencies of 1.4±0.3 Hz (i.e., $\omega/\omega_{ci} = 1.6\pm0.3$) in a $\lambda_{||} = 830$ km wave with $M = 0.96$.

MMS Data Sources and Processing. Particle, magnetic field, and electric field data were measured by the Fast Plasma Investigation[39] (FPI), the Fluxgate Magnetometers[40] (FGM), and Electric Field Double Probe[41] (EDP) instruments, respectively. Corresponding composition data at ~10s time resolution was obtained from the Hot Plasma Composition Analyzer[42] (HPCA). Time series data were high-pass filtered with a 5th order digital Butterworth IIR filter with coefficients b = [0.85850229,-4.29251147,8.58502295,-8.58502295,4.29251147,-0.85850229] and a = [1.0,-4.69504063,8.82614592,-8.30396669,3.90989399,-0.73702619], where b and a correspond to the filter's numerator and denominator polynomials listed in increasing order. This filter had an effective cutoff frequency of 0.5 Hz and no discernable effect (<1%) on the amplitude or phase of a 0.9 Hz input signal.

Data Availability. Data used for this study is available to download from the MMS Science Data Center (https://lasp.colorado.edu/mms/sdc/) or from the corresponding author upon request.

References

1. Alfvén, H. Existence of electromagnetic-hydromagnetic waves. *Nature* 150, 405 (1942)

2. Barnes, A. Collisionless damping of hydrodynamic waves. *Phys. Fluids.* 9, 1483 (1966)

3. Hasegawa, A., & Chen, L, Parametric decay of 'kinetic Alfvén wave' and its application to plasma heating. *Phys. Rev. Lett.* **36**, 1362 (1976).

4. Stix, T. H. *Waves in plasmas.* Am. Inst. of Phys., College Park, Maryland, 566pp (1992)

5. Rezeau, L., Morane, A., Perraut, S., Roux, A., & Schmidt, R. Characterization of Alfvénic fluctuations in the magnetopause boundary layer. *J. Geophys. Res.* 94, 101–110 (1989) doi:10.1029/JA094iA01p00101.

6. Leamon, R. J., Smith, C. W., Ness, N.F., Matthaeus, W.H., & Wong, H.K. Observational constraints on the dynamics of the interplanetary magnetic field dissipation range. *J. Geophys. Res.* 103, 4775–4787 (1998)

7. Sahraoui, F., Goldstein, M.L., Robert, P., & Khotyaintsev, Y. V. Evidence of a Cascade and Dissipation of Solar-Wind Turbulence at the Electron Gyroscale. *Phys. Rev. Lett.* 102, 231102 (2009)

8. Louarn, P. *et al.* Observation of kinetic Alfvèn waves by the Freja spacecraft. *Geophys. Res. Lett.* 21, 1847–1850 (1994)

9. Chaston, C. C. *et al.* Drift-kinetic Alfvén waves observed near a reconnection X line in the Earth's magnetopause. *Phys. Rev. Lett.* 95, 065002 (2005)

10. Seyler, C. E., Wahlund, J.-E., & Holback, B. Theory and simulation of low frequency plasma waves and comparison to Freja satellite observations. *J. Geophys. Res.* 100, 21,453. (1995)

11. Ergun, R. E. *et al.* Localized parallel electric fields associated with inertial Alfvén waves. *Phys. Plas.* 12, 072901 (2005)

12. Chaston, C. C. *et al.* Ionospheric erosion by Alfvén waves. *J. Geophys. Res.* 111, A03206 (2006)

13. Artemyev, A. V., Rankin, R., & Blanco, M. Electron trapping and acceleration by kinetic Alfvén waves in the inner magnetosphere. *J. Geophys. Res.: Space Physics.* 120, 10,305-10,316 (2015)

14. Wong, K.-L. A review of Alfvén eigenmode observations. *Plas. Phys. Cont. Fus.* 4, 1 (1999)

15. Belova, E. V., Gorelenkov, N. N., Fredrickson, E. D., Tritz, K. & Crocker, N. A. Coupling of Neutral-Beam-Driven Compressional Alfvén Eigenmodes to Kinetic Alfvén Waves in NSTX Tokamak and Energy Channeling. *Phys. Rev. Lett.* 115, 015001 (2015)

16. Hollweg, J. V. Kinetic Alfvén wave revisited. *J. Geophys. Res.,* 104,

14811–14819 (1999)

17. O'Neil, T. M. Collisionless Damping of Nonlinear Plasma Oscillations. *Phys. Fluids.* 8, 2255. (1965)
18. Burch, J. L., Moore, T.E., Torbert, R.B., & Giles, B.L. Magnetospheric multiscale overview and science objectives. *Space Sci. Rev.* 199, 5–21 (2015)
19. Cowley, S. W. H. Evidence for the occurrence and importance of reconnection between the Earth's magnetic field and the interplanetary magnetic field, Magnetic Reconnection in Space and Laboratory Plasmas, edited by Hones, E. W. *Geophysical Monograph*. 30, 375–378 (1984)
20. Paschmann, G., *et al.* Plasma acceleration at the Earth's magnetopause: Evidence for magnetic reconnection. *Nature. 282,* 243–246 (1979)
21. Fuselier, S. A. *et al.* Magnetospheric Multiscale science mission profile and operations. *Space Sci. Rev*. 199, 77–103 (2016)
22. Pinçon, J.L., & Glassmeier K.-H., Multi-spacecraft methods of wave field characterization in *Multi-Spacecraft Analysis Methods Revisited*, European Space Agency Publications. Noordwijk, Netherlands (2008)
23. Bellan, P. M. Improved basis set for low frequency plasma waves. *J. Geophys. Res.* 117, A12219 (2012)
24. Bellan, P.M. Revised single-spacecraft method for determining wave vector k and resolving space-time ambiguity. *J. Geophys. Res. Space Physics*. 121, 8589-8599 (2016)
25. Balikhin, M. A., Woolliscroft, L., Alleyne, H., Dunlop, M. & Gedalin, M. A. Determination of the dispersion of low-frequency waves downstream of a quasiperpendicular collisionless shock. *Ann. Geophys.* 15, 143 (1997)
26. Wilson, L. B. III *et al.* Low-frequency whistler waves and shocklets observed at quasi-perpendicular interplanetary shocks. *J. Geophys. Res.* 114, A10106 (2009)
27. Dunlop, M. W., Balogh, A., Glassmeier, K.-H., & Robert, P. Four-point Cluster application of magnetic field analysis tools: The Curlometer. *J. Geophys. Res.* 107, 1384, (2002)
28. Hall, D. S., Chaloner, C.P., Bryant, D.A., Lepine, D. R., & Tritakis, V. P. Electrons in the boundary layers near the dayside magnetopause. *J. Geophys. Res. 96,* 7869–7891 (1991)
29. Sahraoui, F., Goldstein, M.L., Belmont, G., Canu, P., & Rezeau, L. Three Dimensional Anisotropic *k* Spectra of Turbulence at Subproton Scales in the Solar wind. *Phys. Rev. Lett.* 105, 131101 (2010)
30. Salem, C.S. *et al.* Identification of Kinetic Alfvén Wave Turbulence in the Solar Wind. *Ap J Lett*. 745 (2012)
31. André, M. & C. M. Cully. Low-energy ions: A previously hidden solar system particle population*. Geophys. Res. Lett*. 39, L03101 (2012)
32. Manheimer, W. M. Instabilities in a Plasma Coexisting with a Large-Amplitude

Wave. *Phys Rev. A.* 3, 1402 (1971)

33. Ergun, R. E. *et al.* Debye-Scale Plasma Structures Associated with Magnetic- Field-Aligned Electric Fields. *Phys Rev. Lett.* 81, 826 (1998)
34. Che, H. *et al.* A current filamentation mechanism for breaking magnetic field lines during reconnection. *Nature.* 474, 184-187 (2011)
35. Hapgood, M. A. Space physics coordinate transformations: a user guide. *Planet Space Sci.* 40, 711 (1992)
36. Viñas, A., H. K. Wong, and A. J. Klimas. Generation of electron suprathermal tails in the upper solar atmosphere: Implications for coronal heating. *Astrophys. J.* 528, 509 (2000)
37. Olsen, R. C., Scott, L. J., & Boardsen, S. A. Comparison between Liouville's theorem and observed latitudinal distributions of trapped ions in the plasmapause region. *J. Geophys. Res.* 99, 2191–2203 (1994)
38. Chisham, G., Schwartz, S.J., & Burgess,D. The anisotropy variations of electron distributions in the terrestrial ion foreshock. *J. Geophys. Res.* 101, 445–455 (1996)
39. Pollock, C. J. *et al.* Fast plasma investigation for Magnetospheric Multiscale. *Space Sci. Rev.* 199, 331–406 (2016)
40. Russell, C. T. *et al.* The Magnetospheric Multiscale magnetometers. *Space Sci. Rev.* 199, 189–256 (2014)
41. Ergun, R. E. *et al.* The axial double probe and fields signal processing for the MMS mission. *Space Sci. Rev.* 199, 167–188 (2014)
42. Young, D. T. *et al.* Hot plasma composition analyzer for the Magnetospheric Multiscale mission. *Space Sci. Rev.* 199, 407-470 (2014)

End Notes

Acknowledgements. The authors wish to thank the members of the FPI ground operations and science team for their feedback and support and Lynn Wilson for his insights about wave properties. This research was supported by the NASA Magnetospheric Multiscale Mission in association with NASA contract NNG04EB99C and by NSF award 1059519, AFOSR award FA9550-11-1-0184, and DOE awards DE-FG02-04ER54755 and DE-SC0010471. SJS is grateful to the Leverhulme Trust for its award of a Research Fellowship

Author Contributions.
D. J. Gershman conducted the majority of the scientific and data analysis and was responsible for initial preparation of the manuscript text.
A. F-Viñas assisted with the interpretation of wave signatures, plasma wave modeling and with the preparation of the manuscript text.
J.C. Dorelli, S. A. Boardsen and L. A. Avanov assisted with the interpretation of plasma wave signatures, detailed analysis of plasma data, and with the preparation of the manuscript text
P. M. Bellan assisted with the implementation of the wave vector determination method and with the preparation of the manuscript text
S. J. Schwartz assisted with the Liouville mapping of electron data and preparation of the manuscript text.
B. Lavraud, V. N. Coffey, M. O. Chandler, Y. Saito, W. R. Paterson provided and ensured quality of high-resolution plasma data and assisted with the preparation of the manuscript text.
S. A. Fuselier provided and ensured the quality of the plasma composition data.
R. E. Ergun, and R.B. Torbert provided and ensured the quality of high-resolution electric field data and assisted with the preparation of the manuscript text.
R. J. Strangeway and C. T. Russell provided and ensured the quality of high-resolution fluxgate magnetometer data.
B.L. Giles, C. J. Pollock, and J. L. Burch provided institutional and mission-level support of the analysis and ensured overall quality of MMS and FPI data.

Competing Financial Interests. The authors declare no competing financial interests.

Figures and Figure Legends

Figure 1. MMS observations of a reconnection exhaust. (a) Illustration of the MMS constellation near the dayside magnetopause on 30 December 2015. MMS entered a southward flowing reconnection exhaust in the separatrix region on the magnetospheric (msp) side of the magnetopause. (b-i) Plasma parameters from MMS4 across the jet are shown from 22:23-22:30 UT. The density increased to ~10 cm^{-3} (d) and $-V_Z$ increased by ~200 km s^{-1} (e). No rotation in the magnetic field (h) indicated that the spacecraft remained inside the magnetosphere during this time period. ~1 Hz waves (h,i) were observed to be localized in a region of enhanced ion temperature anisotropy, with $T_\perp/T_\| \sim 2$ (f). H^+ dominated the ion composition during this time period.

Figure 2. MMS observations of a KAW packet. Plasma parameters measured by the four MMS observatories on 30 December 2015 in a KAW packet. (a,b) Compressive fluctuations are observed in anti-correlated electron density (Δn_e) and magnetic field magnitude (ΔB) measurements. (c,d) Positively correlated fluctuations are observed in near-transverse components of the magnetic field (ΔB_X) and electron bulk velocity (ΔV_{ex}). (e-h) Fluctuations in both parallel and perpendicular temperature of both electrons (ΔT_e) and ions (ΔT_i) are shown, with the strongest relative fluctuations (~10%) observed in the perpendicular electron temperature. (i) Bursts of electron-scale phase space holes measured in the parallel electric field ($\Delta E_\|$) are bunched with the ion-scale KAW wave and correspond to some of the gradients in the measured electron pressure.

Figure 3. Wavevector estimated from current density fluctuations. (a) Power spectral density of MMS-averaged magnetic field magnitude from 22:26:28.18-22:26:35.83 UT, (b) the imaginary part of the Fourier amplitudes of fluctuations in MMS-averaged **J**x**B**, and (c) corresponding components of **k**(ω) derived using the *Bellan*[23,24] technique. At the spectral peak of ~0.9 Hz, $\mathbf{k} = [7.1\mathrm{x}10^{-3}, -2.0\mathrm{x}10^{-2},-2.2\mathrm{x}10^{-2}]$ km^{-1}. This wavevector yielded $k_\perp\rho_i \sim 1$ and an angle of ~100° with respect to the background magnetic field.

Figure 4. Comparison of current and electric field estimates. (a-c) MMS-averaged current fluctuations ($\Delta\mathbf{J}$) derived from the curlometer technique (blue), four-spacecraft-averaged particle observations (black), and four-spacecraft-averaged plane-wave approximation using $\mathbf{k} = [7.1\mathrm{x}10^{-3}, -2.0\mathrm{x}10^{-2},-2.2\mathrm{x}10^{-2}]$ km^{-1} (red). (d-g) MMS-averaged $\Delta\mathbf{E}_p$ and $\Delta(\mathbf{J}\bullet \mathbf{E}_p)$ derived from the divergence of the electron pressure tensor (blue) and from the plane-wave approximation (red). Agreement between all quantities provides additional confidence in the estimation of **k**.

Figure 5. Modeled dispersion curves for the local plasma environment. (a) The real part of ω/ω_{ci}, i.e., the wave oscillation frequency, (b) the imaginary part of ω/ω_{ci}, i.e., the wave growth/damping rate, and (c) the real part of iE_x/E_y, i.e., the polarization of the wave, as a function of scaled wave-vector magnitude $k\rho_i$. Colored curves correspond to solutions of a linear dispersion relation solver taken along the Alfvén branch for different wavevector angles (θ) relative to the background magnetic field. The fastest growing wave mode has a wavevector parallel/anti-parallel to the background magnetic field (i.e., $\theta = 0^o, 180^o$) at $\omega/\omega_{ci} \sim 0.5$ and $k\rho_i \sim 0.4$ and is left-hand polarized (i.e., $\mathrm{Re}\{iE_x/E_y\} < 0$). A transition to right-hand polarization (i.e., $\mathrm{Re}\{iE_x/E_y\} > 0$) occurred at $\theta \sim 130^o$. No strong growth or damping was predicted for the observed KAW ($\theta = 104 \pm 4^o$, $\omega/\omega_{ci} = 0.61 \pm 0.08$ and $k_\perp\rho_i = 1.02 \pm 0.07$), indicated with the shaded area in panel (a). The dimensions and color of the shaded area correspond to the reported uncertainties of the measured ω/ω_{ci} and $k_\perp\rho_i$ parameters and $\theta \approx 100^o$, respectively Nearby solutions that match two of the measured $\{\omega/\omega_{ci}, k\rho_i, \theta\}$ parameters (but not all three) are shown as solid circles. The color of each circle corresponds to the wavevector angle.

Figure 6. Current and electric field fluctuations in a KAW. Fluctuations in (a) magnetic field magnitude ΔB, (b) parallel electric field $\Delta E_{p||}$ and parallel current $\Delta J_{||}$, (c) $\Delta(J_{||}E_{p||})$, (d-e) perpendicular electric fields ($\Delta E_{p\perp1}$ and $\Delta E_{p\perp2}$) and current ($\Delta J_{\perp1}$ and $\Delta J_{\perp2}$), and (f) $\Delta(J_\perp E_{p\perp})$ observed by MMS4 on 30 December 2015 between 22:26:27 and 22:26:37 UT. Pressure-gradient-driven electric field quantities were inferred from the **k**-vector and electron pressure tensor from MMS4 using the plane-wave approximation (i.e., $\mathbf{E}_p = -i\mathbf{k} \bullet \underline{\mathbf{P}}_e/n_e e$). Current densities were derived directly from MMS4 particle observations. Current density and electric field fluctuations were 90^o out of phase in both the perpendicular and parallel directions, resulting in non-zero instantaneous $\Delta(\mathbf{J} \bullet \mathbf{E}_p)$, which provided confirmation of the conservative energy-exchange between the wave field and plasma particles. The amplitude of $\Delta(J_\perp E_{p\perp})$ was an order of magnitude higher than $\Delta(J_{||}E_{p||})$. The wave-averaged $\Delta(\mathbf{J} \bullet \mathbf{E}_p)$ was approximately zero, indicating that the wave was in a marginally stable state, i.e., was neither growing or damping. Quantities are shown in magnetic coordinates.

Figure 7. Structure inside of a KAW packet. Profile of (a) density n_e, (b) perpendicular electron temperature $T_{e\perp}$, (c) magnetic field magnitude B, (d) parallel electric field $\Delta E_{p||}$ inferred from electron pressure gradients, and (e) parallel potential Φ integrated from $\Delta E_{p||}$ as a function of position D in the wave for MMS4 from 22:26:29.94-22:26:30.90 UT. The reference value for the potential (Φ =0) was taken at the center of the wave, i.e., at the magnetic minimum. The wave had a parallel wavelength of $\lambda_{||}$~830 km or ~20 ρ_i. The ratio of the minimum to maximum magnetic field magnitude was $B_{min}/B_{max} = 0.96$, which was sufficient to trap electrons with magnetic pitch angles between ~75^o and ~105^o. Phase space density as a function of energy and magnetic pitch-angle are shown at the magnetic (f) maximum ($D = 0$) and (g) at the magnetic minimum ($D = \lambda_{||}/2$) in the wave frame of reference (i.e., all measured velocities shifted by $-V_A$ along the magnetic field direction). An illustration of three corresponding populations of electrons is shown in $V_{||}$-$V_\perp$ space in (h). Thermal (energies below $T_e \approx 35$eV) electrons have nearly isotropic pitch-angle distributions (blue contours). Suprathermal (energies above T_e) electrons were observed as peaks in the phase space density at pitch-angles near 0^o and 180^o (red contours). Finally, a trapped population with energies above T_e is shown between the dashed vertical lines (purple contours). These trapped electrons were responsible for the increased perpendicular temperature at the magnetic minima, and accounted for ~50% of the increase in density.

Figure 8. Lioville-mapped electrons in a KAW. Measured phase space densities from MMS4 as a function of magnetic pitch angle and position in the wave, *D,* between successive magnetic field maxima in the KAW packet from Fig. 3 (22:26:29.94-22:26:30.90 UT) for 132eV electrons. Liouville-mapped distributions are shown for $|\Phi|_{max}$ = 0V, 5V, 10V, 15V, 20V, and 25V (a-g). These distributions were constructed using measured phase space densities at the magnetic minimum (i.e., $D = \lambda_{||}/2$). The mirror ratio of $B_{min}/B_{max} = 0.96$ confined particles to pitch-angles between 75^o and 105^o in all cases. The parallel potential formed from $\Delta E_{p||}$ provided additional spatial localization of the trapped population within the wave minima. Vertical dashed lines denote the full-width at half-maximum along D at a pitch-angle of 90^o. The best agreement with the measured data occurred for the distribution mapped using $|\Phi|_{max}$ = 10V, which was consistent with independent estimates of $k_{||}$ and $\Delta E_{p||}$.

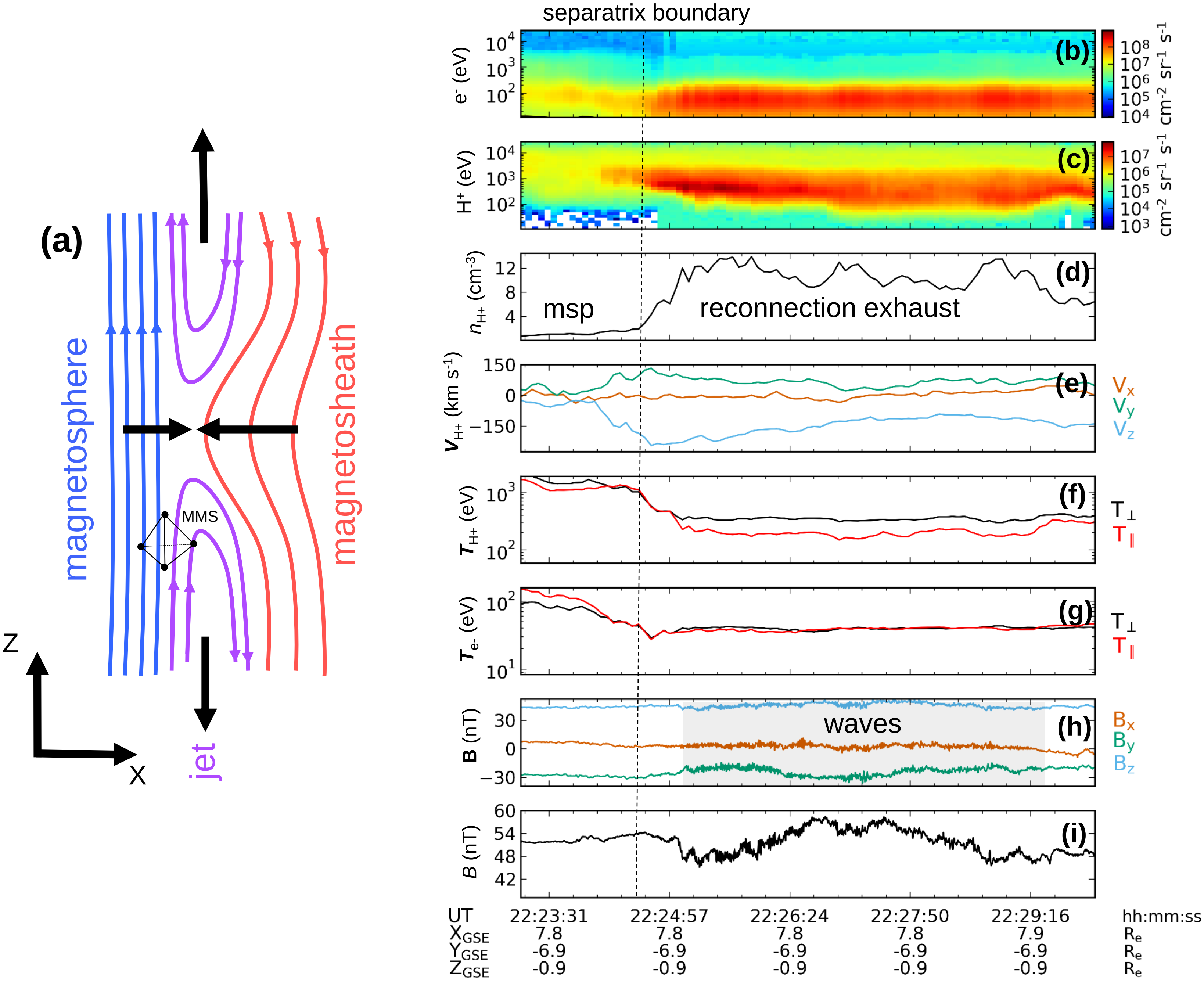
separatrix boundary
(a)
magnetosphere
magnetosheath
MMS
jet
Z
X
(b)
e⁻ (eV)
10⁴
10³
10²
10⁸
10⁷
10⁶
10⁵
10⁴
cm⁻² sr⁻¹ s⁻¹
(c)
H⁺ (eV)
10⁷
10⁶
10⁵
10⁴
10³
cm⁻² sr⁻¹ s⁻¹
(d)
n_H+ (cm⁻³)
12
8
4
msp
reconnection exhaust
(e)
V_H+ (km s⁻¹)
150
0
−150
Vx
Vy
Vz
(f)
T_H+ (eV)
10³
10²
T⊥
T∥
(g)
T_e- (eV)
10²
10¹
T⊥
T∥
(h)
B (nT)
30
0
−30
waves
Bx
By
Bz
(i)
B (nT)
60
54
48
42
UT 22:23:31 22:24:57 22:26:24 22:27:50 22:29:16 hh:mm:ss
XGSE 7.8 7.8 7.8 7.8 7.9 Re
YGSE -6.9 -6.9 -6.9 -6.9 -6.9 Re
ZGSE -0.9 -0.9 -0.9 -0.9 -0.9 Re

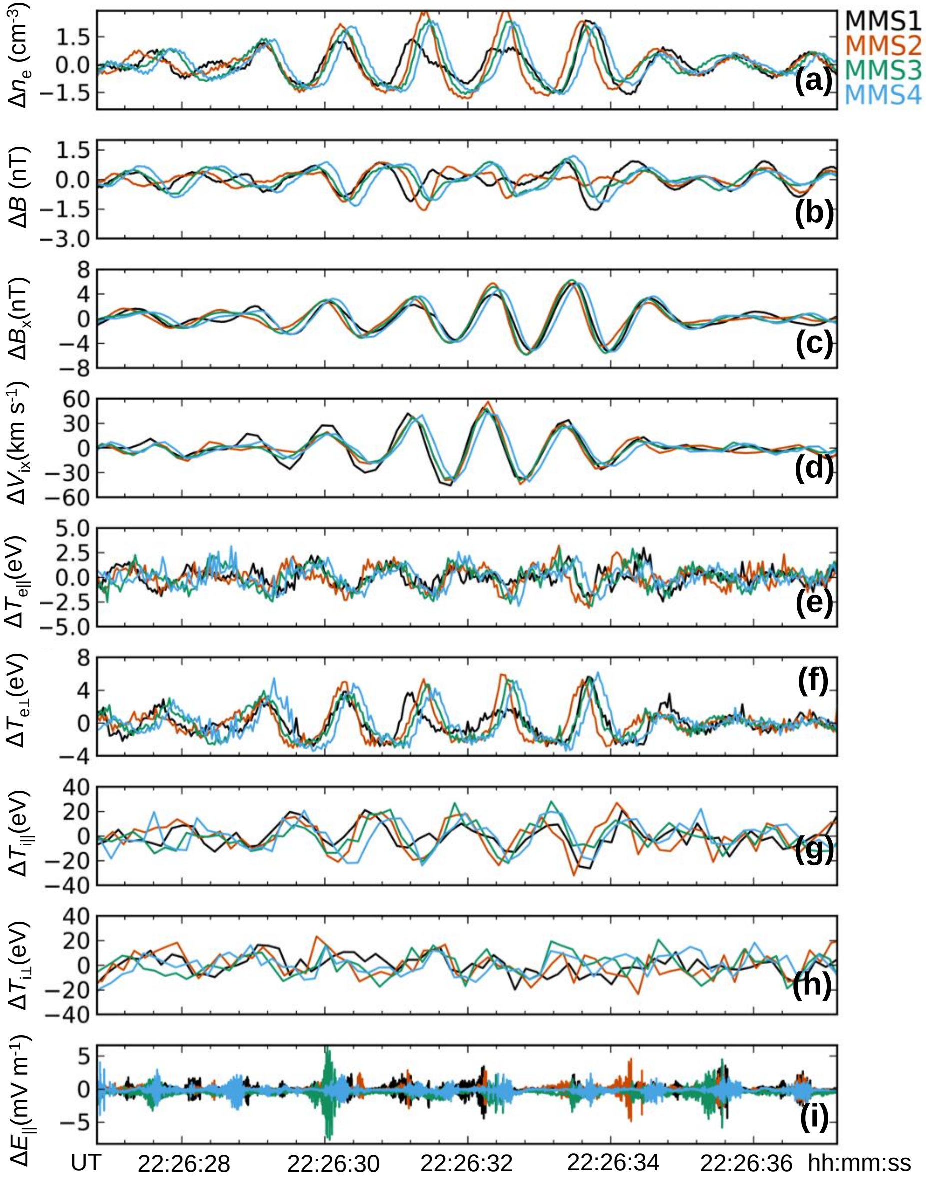
MMS1
MMS2
MMS3
MMS4
Δn_e (cm^{-3})
1.5
0.0
−1.5
(a)
ΔB (nT)
1.5
0.0
−1.5
−3.0
(b)
ΔB_x(nT)
8
4
0
−4
−8
(c)
ΔV_{ix}(km s^{-1})
60
30
0
−30
−60
(d)
Δ$T_{e\|}$(eV)
5.0
2.5
0.0
−2.5
−5.0
(e)
Δ$T_{e\perp}$(eV)
8
4
0
−4
(f)
Δ$T_{i\|}$(eV)
40
20
0
−20
−40
(g)
Δ$T_{i\perp}$(eV)
40
20
0
−20
−40
(h)
Δ$E_\|$(mV m^{-1})
5
0
−5
(i)
UT
22:26:28
22:26:30
22:26:32
22:26:34
22:26:36
hh:mm:ss

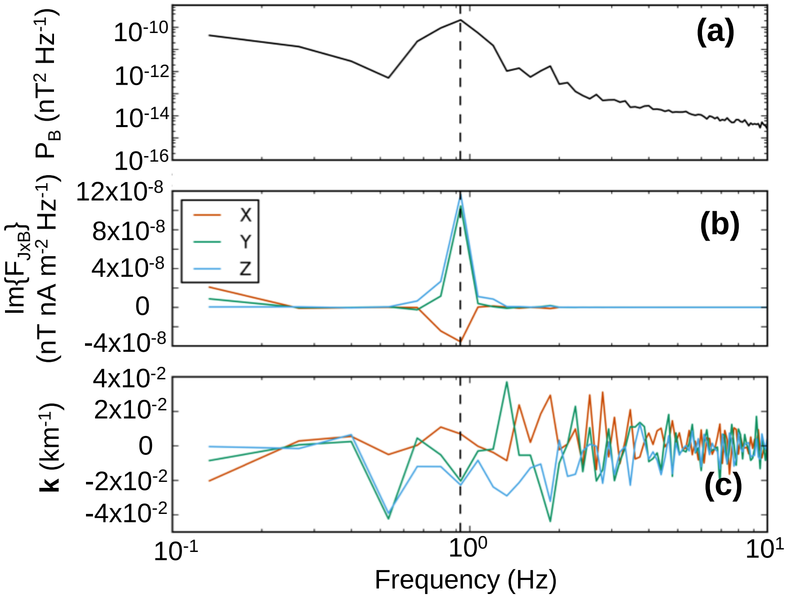
(a)
P_B (nT² Hz⁻¹)
10⁻¹⁰
10⁻¹²
10⁻¹⁴
10⁻¹⁶
(b)
Im{F_JxB}
(nT nA m⁻² Hz⁻¹)
12x10⁻⁸
8x10⁻⁸
4x10⁻⁸
0
-4x10⁻⁸
X
Y
Z
(c)
k (km⁻¹)
4x10⁻²
2x10⁻²
0
-2x10⁻²
-4x10⁻²
10⁻¹
10⁰
10¹
Frequency (Hz)

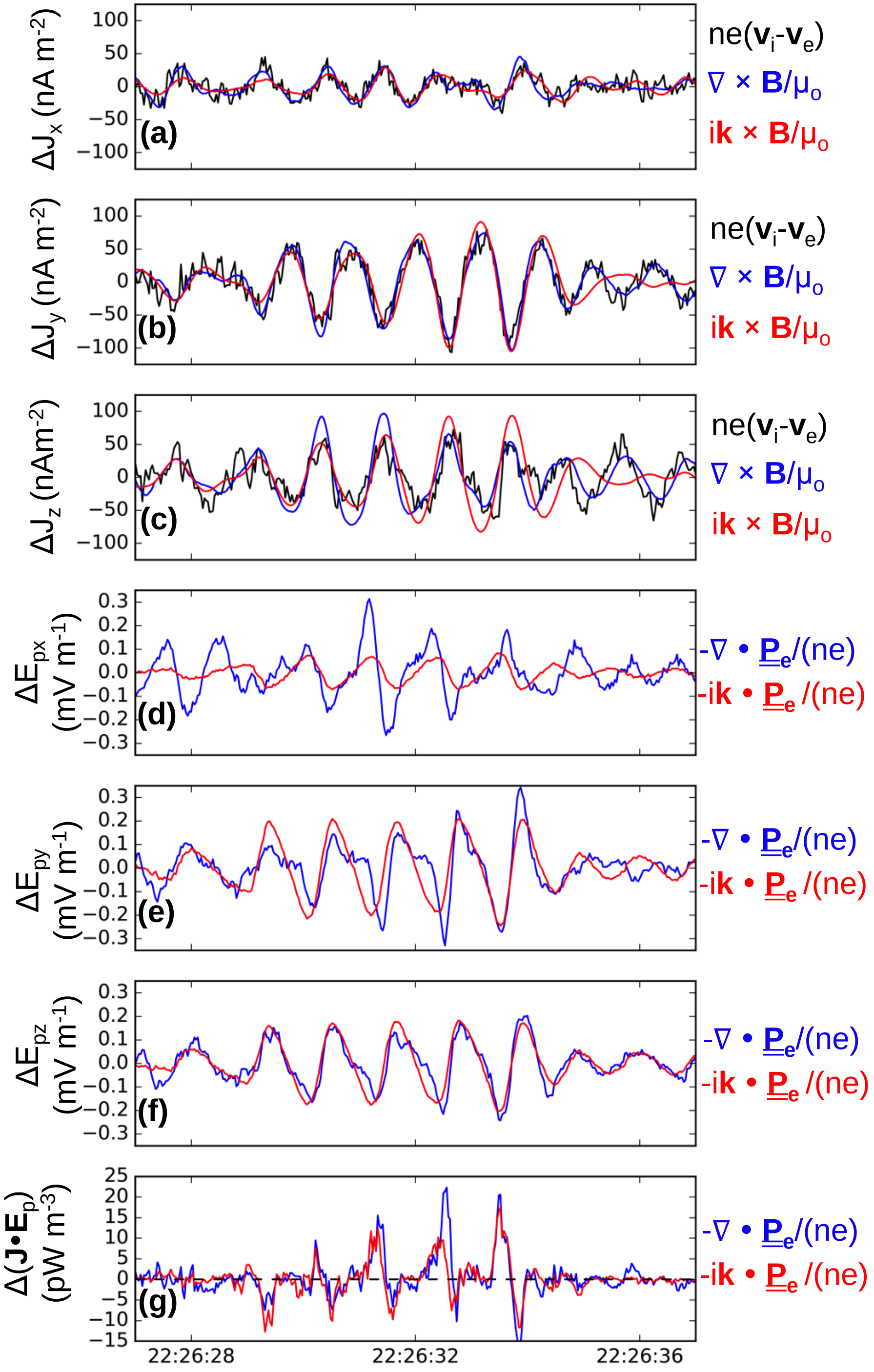
ΔJ_x (nA m^{-2})
100
50
0
−50
−100
(a)
ne($\mathbf{v}_i$-$\mathbf{v}_e$)
$\nabla \times \mathbf{B}/\mu_o$
$\mathbf{ik} \times \mathbf{B}/\mu_o$
ΔJ_y (nA m^{-2})
100
50
0
−50
−100
(b)
ne($\mathbf{v}_i$-$\mathbf{v}_e$)
$\nabla \times \mathbf{B}/\mu_o$
$\mathbf{ik} \times \mathbf{B}/\mu_o$
ΔJ_z (nAm^{-2})
100
50
0
−50
−100
(c)
ne($\mathbf{v}_i$-$\mathbf{v}_e$)
$\nabla \times \mathbf{B}/\mu_o$
$\mathbf{ik} \times \mathbf{B}/\mu_o$
ΔE_{px} (mV m^{-1})
0.3
0.2
0.1
0.0
−0.1
−0.2
−0.3
(d)
$-\nabla \bullet \underline{\mathbf{P}}_\mathbf{e}$/(ne)
$-\mathbf{ik} \bullet \underline{\mathbf{P}}_\mathbf{e}$ /(ne)
ΔE_{py} (mV m^{-1})
0.3
0.2
0.1
0.0
−0.1
−0.2
−0.3
(e)
$-\nabla \bullet \underline{\mathbf{P}}_\mathbf{e}$/(ne)
$-\mathbf{ik} \bullet \underline{\mathbf{P}}_\mathbf{e}$ /(ne)
ΔE_{pz} (mV m^{-1})
0.3
0.2
0.1
0.0
−0.1
−0.2
−0.3
(f)
$-\nabla \bullet \underline{\mathbf{P}}_\mathbf{e}$/(ne)
$-\mathbf{ik} \bullet \underline{\mathbf{P}}_\mathbf{e}$ /(ne)
$\Delta(\mathbf{J} \bullet \mathbf{E}_p)$ (pW m^{-3})
25
20
15
10
5
0
−5
−10
−15
(g)
$-\nabla \bullet \underline{\mathbf{P}}_\mathbf{e}$/(ne)
$-\mathbf{ik} \bullet \underline{\mathbf{P}}_\mathbf{e}$ /(ne)
22:26:28
22:26:32
22:26:36

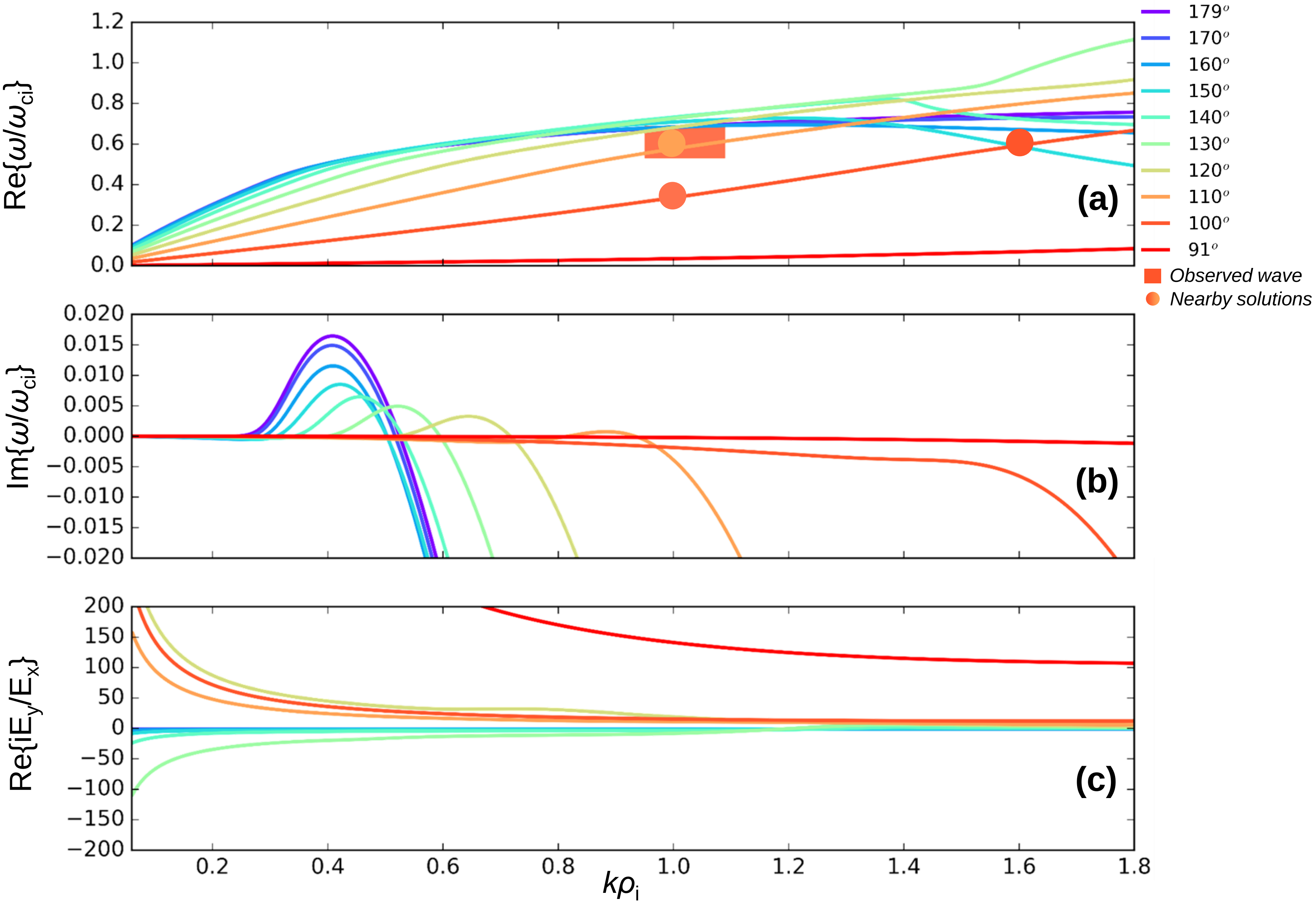
Re{ω/ω_ci}
1.2
1.0
0.8
0.6
0.4
0.2
0.0
(a)
179°
170°
160°
150°
140°
130°
120°
110°
100°
91°
Observed wave
Nearby solutions
Im{ω/ω_ci}
0.020
0.015
0.010
0.005
0.000
−0.005
−0.010
−0.015
−0.020
(b)
Re{iE_y/E_x}
200
150
100
50
0
−50
−100
−150
−200
(c)
0.2
0.4
0.6
0.8
1.0
1.2
1.4
1.6
1.8
kρ_i

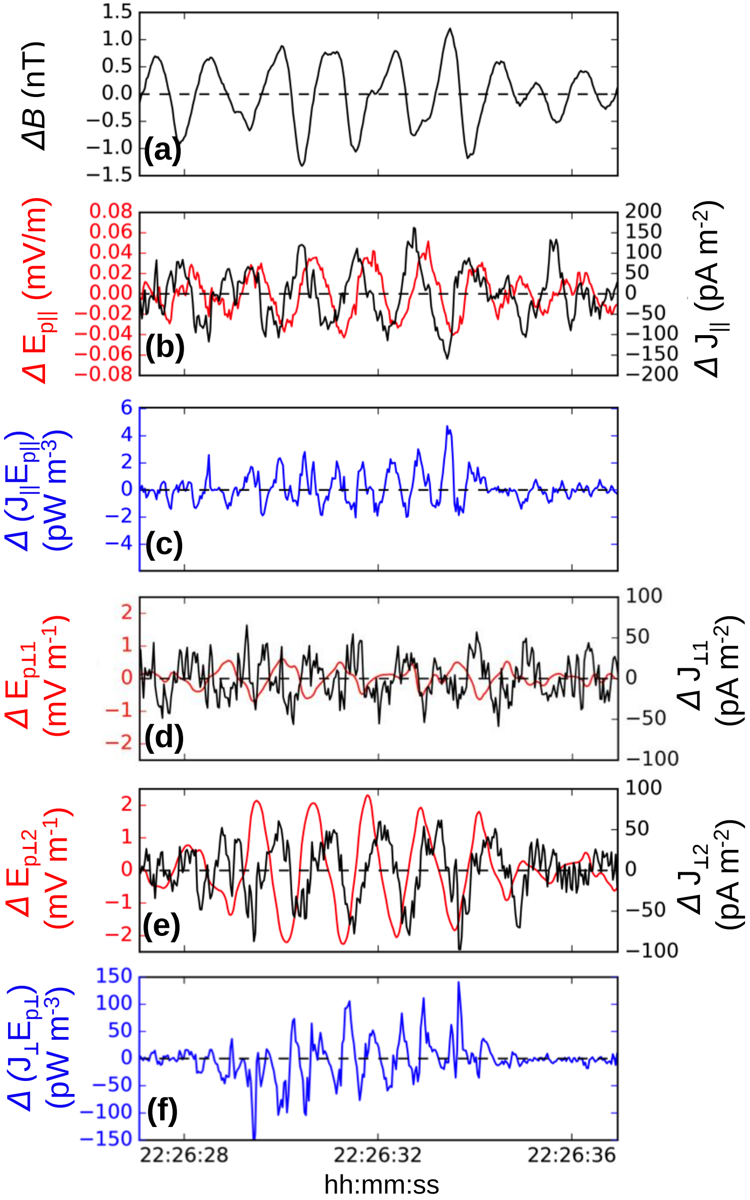
ΔB (nT)
(a)
1.5
1.0
0.5
0.0
−0.5
−1.0
−1.5
ΔE_p‖ (mV/m)
Δ J‖ (pA m-2)
(b)
0.08
0.06
0.04
0.02
0.00
−0.02
−0.04
−0.06
−0.08
200
150
100
50
0
−50
−100
−150
−200
Δ (J‖E_p‖) (pW m-3)
(c)
6
4
2
0
−2
−4
Δ E_p⊥1 (mV m-1)
Δ J⊥1 (pA m-2)
(d)
2
1
0
−1
−2
100
50
0
−50
−100
Δ E_p⊥2 (mV m-1)
Δ J⊥2 (pA m-2)
(e)
2
1
0
−1
−2
100
50
0
−50
−100
Δ (J⊥E_p⊥) (pW m-3)
(f)
150
100
50
0
−50
−100
−150
22:26:28
22:26:32
22:26:36
hh:mm:ss

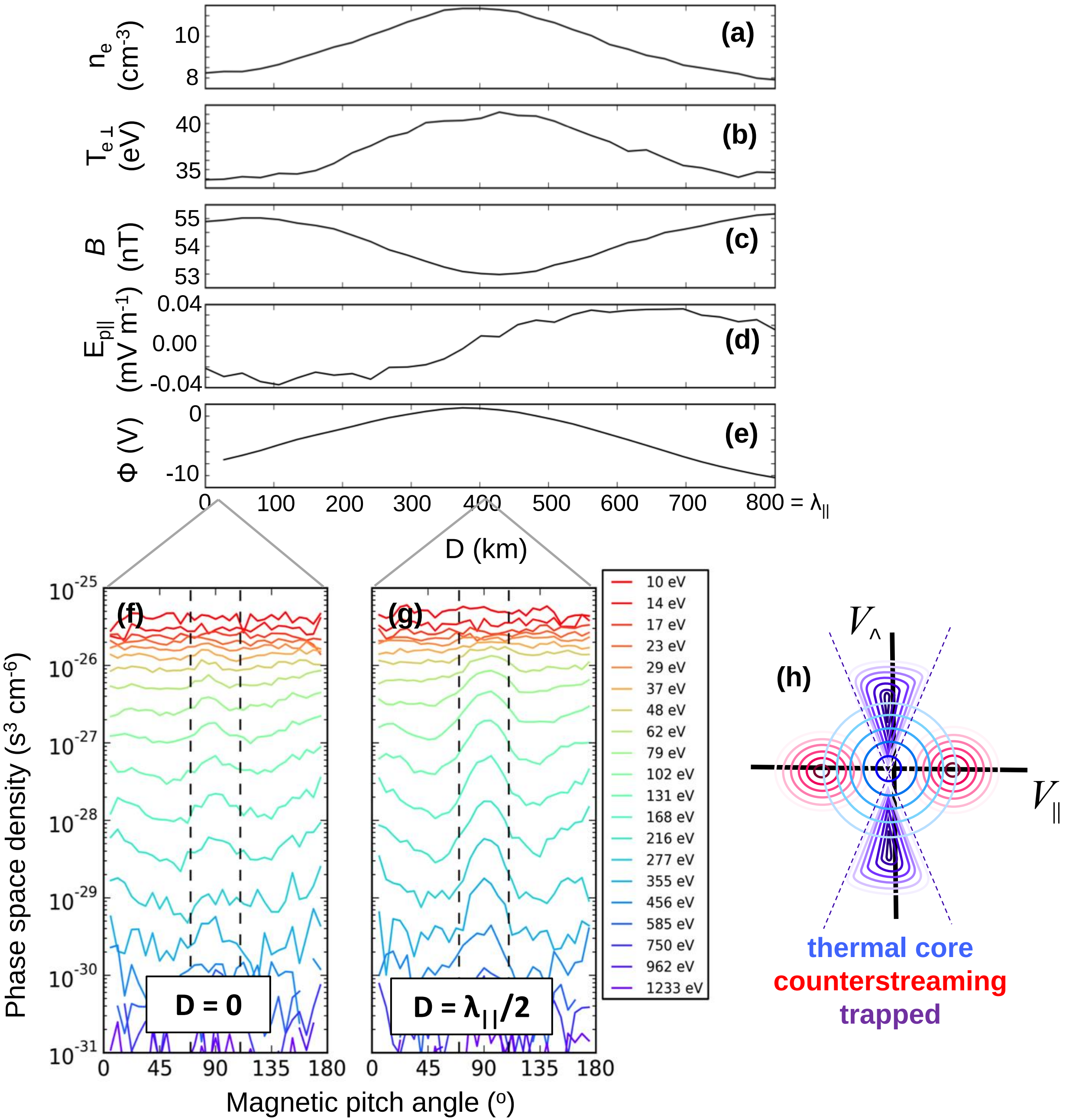

n_e (cm^{-3})
10
8
(a)
$T_{e\perp}$ (eV)
40
35
(b)
B (nT)
55
54
53
(c)
$E_{p\parallel}$ (mV m^{-1})
0.04
0.00
-0.04
(d)
Φ (V)
0
-10
(e)
0
100
200
300
400
500
600
700
800 = $\lambda_\parallel$
D (km)
Phase space density (s^3 cm^{-6})
10^{-25}
10^{-26}
10^{-27}
10^{-28}
10^{-29}
10^{-30}
10^{-31}
(f)
D = 0
(g)
D = $\lambda_{||}/2$
0
45
90
135
180
Magnetic pitch angle (°)
10 eV
14 eV
17 eV
23 eV
29 eV
37 eV
48 eV
62 eV
79 eV
102 eV
131 eV
168 eV
216 eV
277 eV
355 eV
456 eV
585 eV
750 eV
962 eV
1233 eV
(h)
$V_\perp$
$V_\parallel$
thermal core
counterstreaming
trapped

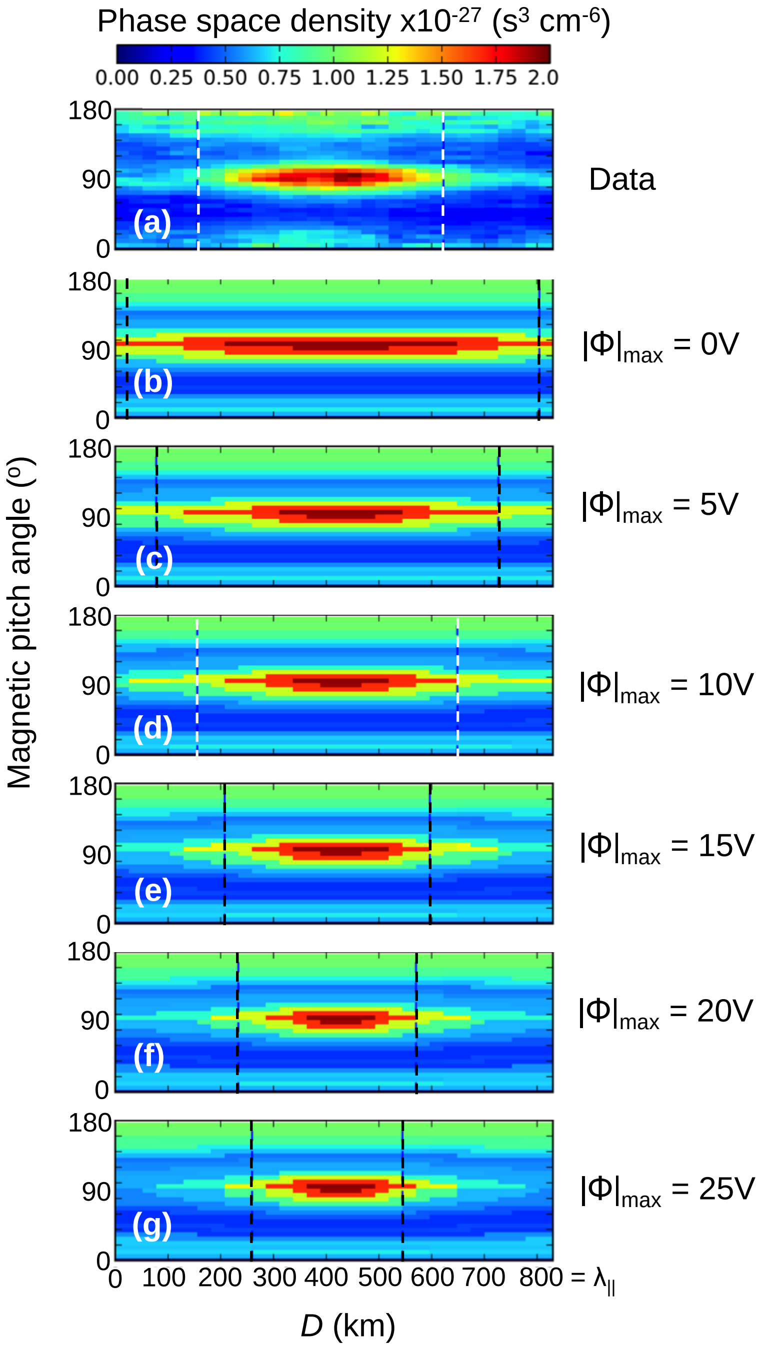
Phase space density x10^{-27} (s^3 cm^{-6})
0.00 0.25 0.50 0.75 1.00 1.25 1.50 1.75 2.0
Magnetic pitch angle (°)
180
90
0
(a)
Data
(b)
$|\Phi|_{max}$ = 0V
(c)
$|\Phi|_{max}$ = 5V
(d)
$|\Phi|_{max}$ = 10V
(e)
$|\Phi|_{max}$ = 15V
(f)
$|\Phi|_{max}$ = 20V
(g)
$|\Phi|_{max}$ = 25V
0 100 200 300 400 500 600 700 800 = $\lambda_{||}$
D (km)